Tidally induced variations of polar mesospheric cloud altitudes and ice water content using a data assimilation system

Michael H. Stevens,[1] David E. Siskind,[1] Stephen D. Eckermann,[1] Lawrence Coy,[1] John P. McCormack,[1] Christoph R. Englert,[1] Karl W. Hoppel,[2] Kim Nielsen,[3] Andrew J. Kochenash,[3] Mark E. Hervig,[4] Cora E. Randall,[5] Jerry Lumpe,[6] Scott M. Bailey,[7] Markus Rapp,[8] and Peter Hoffmann[8]

Received 18 September 2009; revised 4 May 2010; accepted 6 May 2010; published 24 September 2010.

[1] A variety of spaceborne experiments have observed polar mesospheric clouds (PMC) since the late 20th century. Many of these experiments are on satellites in Sun-synchronous orbits and therefore allow observations only at fixed local times (LT). Temperature oscillations over the diurnal cycle are an important source of PMC variability. In order to quantify long-term natural or anthropogenic changes in PMCs, it is therefore essential to understand their variation over the diurnal cycle. To this end, we employ a prototype global numerical weather prediction system that assimilates satellite temperature and water vapor observations from the ground to ~90 km altitude. We assemble the resulting 6 hourly high-altitude meteorological assimilation fields from June 2007 in both LT and latitude and use them to drive a one-dimensional PMC formation model with cosmic smoke serving as nucleation sites. We find that there is a migrating diurnal temperature tide at 69°N with a variation of ±4 K at 83 km, which controls the variation of PMC total ice water content (IWC) over the diurnal cycle. The calculated IWC is normalized to observations at 2300 LT by the Solar Occultation for Ice Experiment and allowed to vary with temperature over the diurnal cycle. We find that the IWC at 69°N has a single maximum between 0700 and 0800 LT and a minimum between 1900 and 2200 LT and varies by at least a factor of 5. The calculated variation of IWC with LT is substantially larger at 57°N, with a single prominent peak near 0500 LT.

Citation: Stevens, M. H., et al. (2010), Tidally induced variations of polar mesospheric cloud altitudes and ice water content using a data assimilation system, *J. Geophys. Res.*, *115*, D18209, doi:10.1029/2009JD013225.

1. Introduction

[2] Polar mesospheric clouds (PMCs) are tenuous layers of ice particles that form near 83 km altitude over the summer polar region. When observed from the ground, they are also known as noctilucent clouds (NLCs) by their glowing appearance as observed against the twilight sky. We hereinafter refer to all mesospheric clouds as PMCs for consistency. Some analyses of satellite observations over the past 30 years suggest that PMCs have become more frequent [e.g., *Shettle et al.*, 2009] and brighter [e.g., *Thomas et al.*, 2003; *DeLand et al.*, 2003], fueling the suggestion that they are indicators of global climate change [*Thomas et al.*, 1989; *Thomas*, 1996].

[3] Ground-based observations indicate that PMCs exhibit tidally induced variations in brightness, altitude and occurrence frequency [*von Zahn et al.*, 1998; *Chu et al.*, 2003, 2006; *Fiedler et al.*, 2005]. On the other hand, PMC observations are typically from satellites in Sun-synchronous orbits measuring at discrete local times (LT) during any given season. This is important because ground-based observations of brightness variations at a fixed location vary over the diurnal cycle by ±20% or more [*von Zahn et al.*, 1998; *Fiedler et al.*, 2005], yet reported multidecadal PMC albedo trends are less than 1%/yr [e.g., *DeLand et al.*, 2007]. Constraining PMC secular variations clearly requires a quantitative understanding of diurnal effects so that inferred trends are uncontaminated by diurnal variations [*Stevens et al.*, 2007; *Kirkwood et al.*, 2008]. This is especially important for the suite of solar backscattered ultraviolet (SBUV) instruments, which have measured PMCs continuously from Sun-synchronous orbits at a variety of fixed LT for over 30 years. For Northern

[1]Space Science Division, Naval Research Laboratory, Washington, District of Columbia, USA.
[2]Remote Sensing Division, Naval Research Laboratory, Washington, District of Columbia, USA.
[3]Computational Physics, Inc., Springfield, Virginia, USA.
[4]GATS, Inc. Driggs, Idaho, USA.
[5]Laboratory for Atmospheric and Space Physics and Department of Atmospheric and Oceanic Sciences, University of Colorado, Boulder, Colorado, USA.
[6]Computational Physics, Inc., Boulder, Colorado, USA.
[7]Bradley Department of Electrical and Computer Engineering, Virginia Polytechnical and State University, Blacksburg, Virginia, USA.
[8]Leibniz Institute of Atmospheric Physics e.V., Kühlungsborn, Germany.

Copyright 2010 by the American Geophysical Union.
0148-0227/10/2009JD013225

Hemisphere data, these SBUV LT are biased almost exclusively to the morning from about 1979 to 1990 and then distributed approximately equally over the diurnal cycle from 1990 to the present [*DeLand et al.*, 2007].

[4] One useful measure of PMC variability is the ice mass column density, sometimes called the total ice water content (IWC) [*Thomas and McKay*, 1985; *Stevens et al.*, 2005; *Rapp and Thomas*, 2006; *Stevens et al.*, 2007; *Hervig et al.*, 2009a, 2009b]. The IWC is the vertically integrated ice mass density and therefore a direct measure of the total ice present in a PMC layer. A quantitative simulation of IWC over the diurnal cycle requires knowledge of the ambient conditions with LT.

[5] We herein determine tidal variations of temperature, water vapor, and winds over the diurnal cycle using meteorological analyses produced by the data assimilation component of the Advanced-Level Physics High-Altitude (ALPHA) Navy Operational Global Atmospheric Prediction System (NOGAPS) in order to simulate variations in IWC with LT. In section 2, we describe how we use the NOGAPS-ALPHA analysis for June 2007 to drive a one-dimensional microphysical model and to simulate the diurnal variation of IWC. In section 3, we compare the results at 69°N with IWC observations at discrete LT by the Solar Occultation for Ice Experiment (SOFIE) and the Cloud Imaging and Particle Size (CIPS) instrument on the NASA Aeronomy of Ice in the Mesosphere (AIM) satellite [*Russell et al.*, 2009; *Hervig et al.*, 2009a] as well as the Student Nitric Oxide Explorer (SNOE) [*Bailey et al.*, 2005]. We also compare the model IWC results at 57°N with cloud occurrence frequency observations over the diurnal cycle by the Spatial Heterodyne Imager for Mesospheric Radicals (SHIMMER) [*Englert et al.*, 2008; *Stevens et al.*, 2009]. In section 4, we show tidal variations at PMC altitudes over three successive northern seasons and discuss the implications of all our results for long-term trend analyses.

2. Modeling Approach

[6] Our modeling approach is designed to quantify the effects of migrating tides on heavily averaged PMC observations in the Northern Hemisphere. This study therefore does not address the geographical variability of ice layers [*Berger and Lübken*, 2006], hemispheric differences of PMCs [e.g., *Bailey et al.*, 2007; *Lübken and Berger*, 2007] or the modeling of long-term PMC variability [*Lübken et al.*, 2009]. We focus instead on how PMCs vary with LT in the Arctic so that small long-term changes inferred from existing satellite data sets fixed in LT may be uncoupled from diurnal variations. This may benefit the identification of any source of long-term PMC change.

[7] We first describe the ambient conditions over both latitude and LT and then use this time history to drive a one-dimensional microphysical model. To estimate the meridional transport of the ice particles, we use back trajectories based upon NOGAPS-ALPHA analyzed horizontal winds. These trajectories and hence source regions vary with LT since the wind field varies with LT. Starting from the source region for the target LT and latitude of interest, we integrate forward in time to drive the one-dimensional Community Aerosol and Radiation Model for Atmospheres (CARMA) [*Rapp and Thomas*, 2006] from which the PMC properties are calculated.

[8] The calculated IWC is a function of how long the ice particles are subjected to temperatures below the frost point. This particle "lifetime" may be related to processes we do not consider, such as gravity wave activity, and is therefore not well constrained by our model. However, we use the SOFIE IWC observations as a point of reference at 2300 LT, and we adjust the model ice particle lifetime to agree with these data. To do this we introduce a warm bias to the model and cool the model atmosphere to ambient conditions so that the resultant ice particle growth yields an IWC equal to SOFIE IWC observations at 2300 LT. To model the diurnal variation of PMCs, we use 24 trajectories, one for each hour of LT, and use the same lifetime for each simulation. In the following two subsections, we first describe our composite wind and temperature fields from NOGAPS-ALPHA. We then discuss their use to drive CARMA.

2.1. NOGAPS-ALPHA

[9] NOGAPS-ALPHA is a nonoperational research prototype of the U. S. Navy's operational global numerical weather prediction system that extends its vertical range to ~90 km altitude, allowing us to simulate the PMCs near 83 km. Unlike climate models, this system is focused on accurate "nowcasting" and short-term forecasting of the global atmosphere. The system consists of two main components: a global forecast model that predicts future atmospheric conditions and a three-dimensional variational data assimilation system (NAVDAS: NRL Atmospheric Variational Data Assimilation System) that provides synoptic initial conditions for those forecasts based on available observations. The two components work synergistically in a coupled forecast-assimilation update cycle, with forecasts providing an estimate of the global atmospheric state that are updated every 6 h by the assimilation of global observations. Our focus in this work is on the global analysis fields in the polar summer mesosphere provided by the assimilation of mesospheric observations into the NOGAPS-ALPHA system.

[10] NOGAPS-ALPHA analysis fields have been extended upward by assimilating high-altitude observations from research satellites, in addition to the usual complement of operational sensor data at lower altitudes. Middle atmosphere temperature and water vapor observations are assimilated from the Microwave Limb Sounder (MLS) on the Aura satellite and the Sounding of the Atmosphere using Broadband Emission Radiometry (SABER) instrument on the Thermosphere Ionosphere Mesosphere Energetics and Dynamics (TIMED) satellite. The vertical resolution of the SABER temperature observations is ~2 km [*Remsberg et al.*, 2008] and the vertical resolution of the MLS temperature and water vapor retrievals is ~10–12 km near 80 km altitude [*Lambert et al.*, 2007; *Schwartz et al.*, 2008]. *Hoppel et al.* [2008] described initial experiments for January 2006 that extended the analyses to 0.01 hPa by assimilating MLS and SABER temperatures. *Eckermann et al.* [2009] extended the system by assimilating newer versions of the temperature retrievals up to 0.002 hPa, in addition to MLS water vapor and ozone. It is these latter analysis fields that we use in the present work.

[11] The effective horizontal resolution of this NOGAPS-ALPHA analysis is approximately 2° latitude × 2° longitude, although the output is interpolated onto a 1° × 1° isobaric grid. The assimilated temperature fields in the summer polar mesosphere revealed good agreement with independent satellite observations [*Eckermann et al.*, 2009, Figure 2]. Furthermore, saturation ratios derived diagnostically from assimilated temperature and humidity fields exhibited excellent agreement with PMCs observed from the ground, from SOFIE, and from SHIMMER [*Eckermann et al.*, 2009].

[12] The geophysical variability of the horizontal winds is ~20 m/s from one 6 h update cycle to the next and the geophysical variability of the temperatures is ~5 K, which combine to yield unreasonably large uncertainties in our back trajectories and cloud simulations. To reduce the variability, we average the NOGAPS-ALPHA synoptic fields of temperature, water vapor, and horizontal and vertical winds on a LT grid for all of June 2007. This month is chosen because it is during the TIMED yaw cycle that includes north-looking SABER data, thereby maximizing the amount of assimilated temperature data in the polar summer. This June average of 120 6 hourly assimilation update cycles removes all longitudinal variability and instead yields fields that isolate the migrating tides, which are now described as a function of latitude and LT only. In this way, we derive representative conditions for the polar summer mesosphere for use in comparisons with longitudinally and seasonally averaged PMC observations.

[13] The average diurnal variations for June 2007 from NOGAPS-ALPHA are shown at 83 km geometric altitude in Figure 1a for temperature and Figure 1b for water vapor with the calculated degree of supersaturation shown in Figure 1c. Although the equilibrium vapor pressure of water vapor over ice at such low temperatures has not been measured directly, our diagnostic supersaturation ratios in Figure 1c use the expression of *Marti and Mauersberger* [1993] as recommended by *Rapp and Thomas* [2006]. From Figure 1a, the temperature at 69°N is on average 143 K, in good agreement with the climatology of *Lübken* [1999], who finds the temperature to be 146 ± 4 K at this altitude in mid-June. A predominantly diurnal oscillation is present in temperature with an amplitude of about 4 K near 69°N, a minimum near 0300 LT and a maximum near 1700 LT, in agreement with the analysis at 60°N of *Eckermann et al.* [2009, Figure 13]. This result from NOGAPS-ALPHA is also in good agreement with independent ground-based temperature observations by *Singer et al.* [2003], who report that the diurnal tide dominates summer mesospheric temperature variability at Arctic latitudes with an amplitude of 3–8 K. Near the equator at 82 km altitude, temperature tides from NOGAPS-ALPHA have larger amplitudes of 5–10 K, in general agreement with data-validated results from the Canadian Middle Atmosphere Model for June [*McClandress*, 2002; *Eckermann et al.*, 2009].

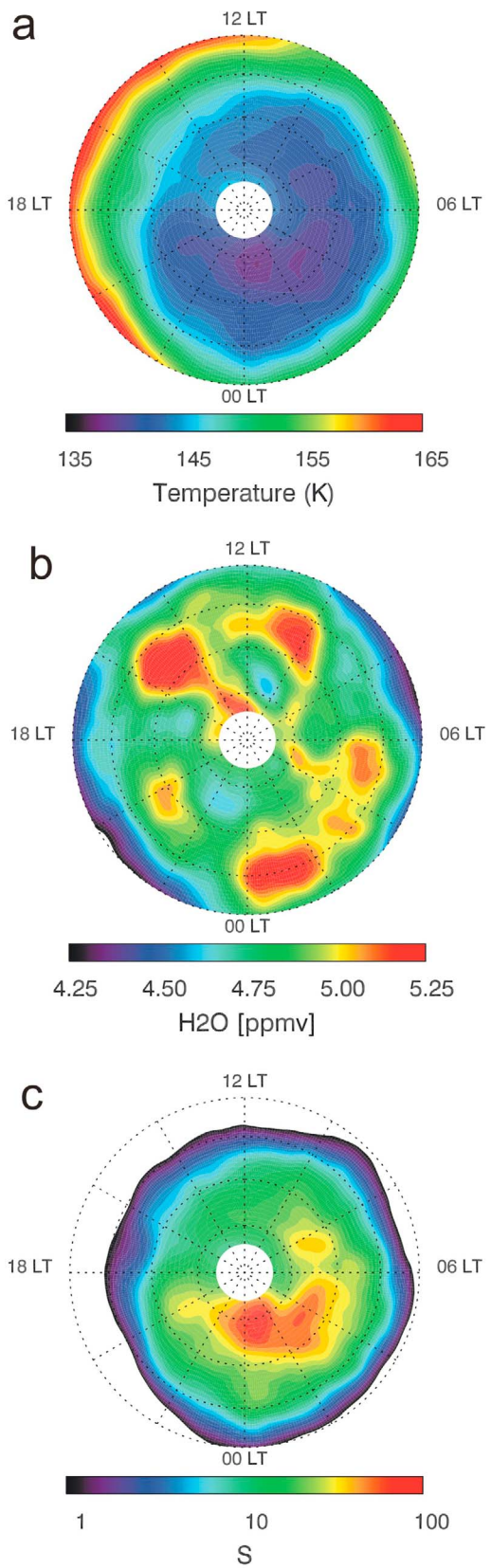

Figure 1. NOGAPS-ALPHA analyses at 83 km geometric altitude and for June 2007. The results for (a) temperature, (b) water vapor, and (c) degree of supersaturation (S) are averaged in LT from 50°N–85°N. Latitudes poleward of 85°N are omitted due to the lack of satellite data. Local midnight is at the bottom of each plot and noon is at the top so that LT progresses counterclockwise around each image. Note that PMCs can exist where $S > 1$.

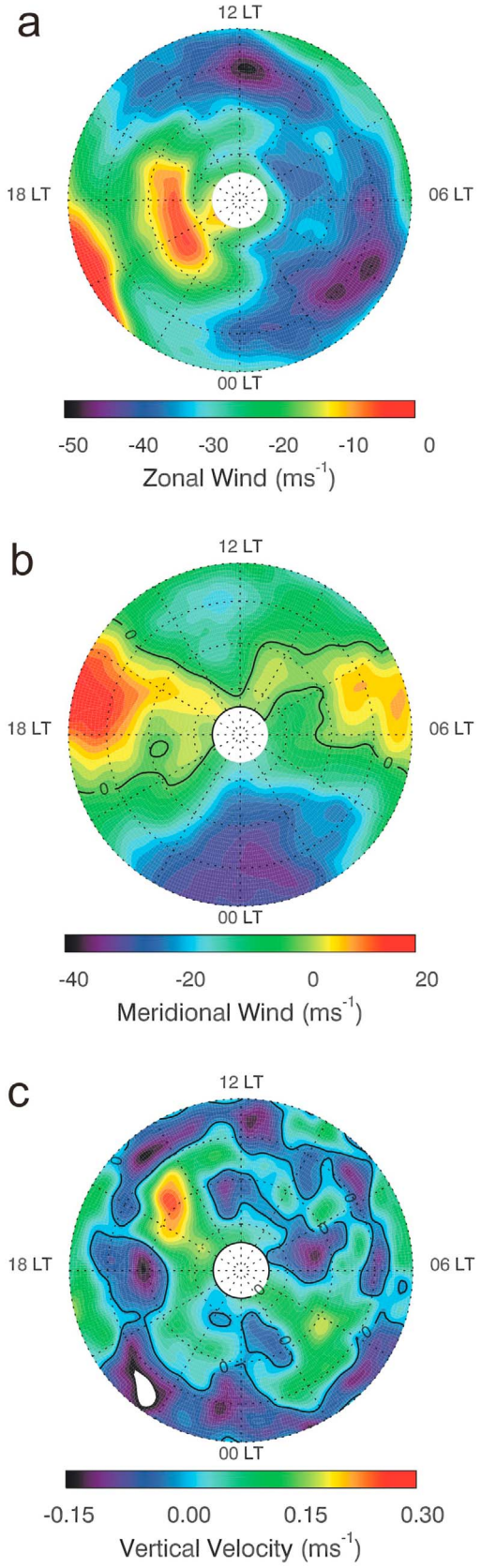

Figure 2. NOGAPS-ALPHA analysis results for (a) zonal winds, (b) meridional winds, and (c) derived vertical winds averaged in LT over June 2007 at 83 km geometric altitude. Positive zonal winds are eastward, positive meridional winds are northward, and positive vertical winds are upward. The zero wind contours are overplotted in Figures 2b and 2c. Latitudes poleward of 85°N are omitted due to lack of data.

[14] The water vapor in Figure 1b shows a slight overall enhancement near 65°N relative to mean values at other latitudes. This enhancement near 65°N was predicted in a modeling study by *von Zahn and Berger* [2003] as being due to equatorward transport of PMCs to warmer regions where the ice sublimates; however, they were unable to verify this prediction with observations. Since the NOGAPS-ALPHA synoptic water vapor analysis is driven by MLS data, our result in Figure 1b can be considered as a validation of the von Zahn and Berger prediction.

[15] The water vapor mixing ratio from NOGAPS-ALPHA in Figure 1b is about 5 ppmv at 69°N and 2300 LT. This is in good agreement with independent SOFIE observations fixed at 2300 LT that show that the water vapor mixing ratio is about 5 ppmv in June 2007 near 83 km altitude [*Gordley et al.*, 2009]. The variation of the NOGAPS-ALPHA water vapor over the diurnal cycle is about ±0.25 ppmv in Figure 1b. This amplitude is smaller than that modeled by von Zahn and Berger who show variations of about ±3 ppmv at 82 km. This difference may be due to the coarse vertical resolution (10–12 km) of the MLS water vapor profiles used in the data assimilation.

[16] The degree of supersaturation (S) calculated from the temperature and water vapor in Figures 1a and 1b, respectively, is shown in Figure 1c. PMCs can exist in regions where $S > 1$ and the low morning temperatures in Figure 1a are reflected in the high degree of saturation during the same time period in Figure 1c. Note that $S > 1$ at all LT poleward of ~60°N.

[17] The derived zonal, meridional, and vertical winds from the NOGAPS-ALPHA analysis are shown in Figures 2a–2c. The vertical winds are calculated diagnostically from the divergence of the horizontal wind fields [*Hogan and Rosmond*, 1991] and peak near 0400 and 1500 LT. The importance of vertical winds in the calculation of mesospheric ice particle properties is discussed in detail by *Berger and von Zahn* [2002]. Note that the NOGAPS-ALPHA absolute vertical wind speeds reach up to 20 cm/s. This is considerably larger than those used by some other previous PMC modeling studies, which show mean vertical winds from 2 to 5 cm/s near 83 km altitude [e.g., *von Zahn and Berger*, 2003; *Siskind et al.*, 2005; *Herbort et al.*, 2007]. We note that ground-based lidar observations near 40°N have indicated a predominantly semidiurnal variation in vertical winds with amplitudes near 30 cm/s in this region of the atmosphere [*Kwon et al.*, 1987]. For comparison, average sedimentation rates of PMC ice particles at 83 km altitude are smaller and around 0.1–6 cm/s [*Klostermeyer*, 1998].

[18] To distinguish the relative amplitudes of the migrating diurnal and semidiurnal tidal component, we have Fourier transformed the temperatures shown in Figure 1a and show the results in Figures 3a and 3b. For these results we have

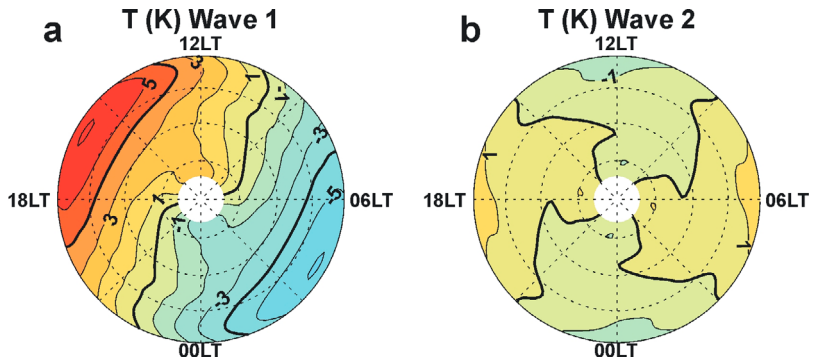

Figure 3. Mean variation with local time and latitude of temperature at 83 km geometric altitude due to (a) the migrating diurnal tide and (b) the migrating semidiurnal tide. Results are monthly means for June 2007. See text for details.

assumed that a 24 h period corresponds exclusively to the wave number 1 solar migrating diurnal tide (Figure 3a) and that a 12 h period corresponds exclusively to the wave number 2 solar migrating semidiurnal tide (Figure 3b). Figure 3a shows that the diurnal tide has the largest amplitude between 50°N and 60°N and dominates over the semidiurnal tide in Figure 3b throughout the PMC region.

[19] To illustrate how pervasive the oscillation of NOGAPS-ALPHA vertical winds is with altitude over the diurnal cycle, Figure 4a shows a cross section of the vertical winds at 69°N over both LT and altitude in the PMC altitude region between 80 and 87 km. The calculated PMC altitudes using CARMA are also shown and are determined by the altitude of maximum ice volume density for each simulation. The PMC altitude varies over the diurnal cycle but on average is near 83 km, consistent with observations and model results [*Lübken et al.*, 2008]. As expected, the PMC altitudes reach a maximum at the node between the maximum upward and downward vertical wind. Figure 4a also illustrates that the strong upward winds near 0400 and 1500 LT are present throughout the upper mesosphere and would help drive the altitude variations of both PMC and polar mesospheric summer echoes (PMSE) in a similar way as is observed from ground-based observations [*von Zahn and Bremer*, 1999; *Hoffmann et al.*, 2008]. Direct comparisons of our model results in Figure 4 to altitude variations over the diurnal cycle from ground-based observations are limited by differences in the ice particle history inherently present in observations at a fixed location such as gravity wave activity, planetary wave activity, and nonmigrating tides.

[20] Figure 4b shows the variations in temperatures over the diurnal cycle for the same altitude region. Note that the PMC altitude variations driven by the vertical winds slightly modify the diurnal oscillation of temperatures on the ice particles compared to oscillations at a fixed altitude surface of 83 km. So although the temperature excursions at 83 km are ±4 K, the temperature excursions to which ice particles are subjected are about ±3 K.

[21] In order to help validate the horizontal and vertical winds shown in Figure 4a, we compare them with ground based horizontal meteor winds observed at 69°N (Andenes, Norway) and 85 km geometric altitude in Figure 5. In addition, we performed five short term integrations of the forecast model component of NOGAPS-ALPHA, initialized at different days spanning the month of June 2007, and present the calculated winds from the third model day of those simulations as an additional curve. A semidiurnal oscillation in both the meridional and zonal component, with a stronger peak later in the day, is evident in all three curves. The agreement between both components of NOGAPS-ALPHA (forecast model and assimilations) and with the observations is very satisfying because the two NOGAPS-ALPHA components derive winds differently. NOGAPS-ALPHA does not assimilate any middle atmospheric wind data directly, but rather, as part of the temperature assimilation, calculates correlated temperature and wind increments based upon a gradient wind approximation in the off-diagonal elements of the background error covariance matrix. The forecast model winds are constrained by the physical parameterizations in the model (e.g., gravity wave drag, diffusion and tides forced by the model at lower altitudes that propagate into the mesosphere). Thus the NOGAPS-ALPHA winds are primarily data driven; the forecast winds are primarily constrained by the model physics. The validation presented in Figure 5 with the meteor radar winds can thus be considered a true three-way intercomparison between two approaches to calculating winds and the Andenes data.

2.2. Ice Particle Trajectories and CARMA

[22] As noted earlier, our approach is a two-step process. We first use the NOGAPS-ALPHA analyzed horizontal winds to calculate hypothetical cloud parcel trajectories at 83 km altitude from a given latitude. We focus herein on two latitudes for which we have data in June 2007: 69°N and 57°N. Contributions from the effects of vertical winds are small so variations on the trajectory due to changes in the ice particle altitude are not included here. Since the prevailing motion of the ice particle is from east to west, a small correction is made to the LT at each time step because the zonal winds are pushing the ice parcels toward earlier LT. For an average westward wind of 30 m/s, this correction amounts to about 10 min/h at 69°N.

[23] The second step uses CARMA to simulate PMC formation and growth. We integrate forward in time along the trajectory and use the appropriate temperature and vertical wind fields at each time step as inputs to CARMA. CARMA has been used in many previous PMC studies, and we use the same version as that used in the work of *Rapp*

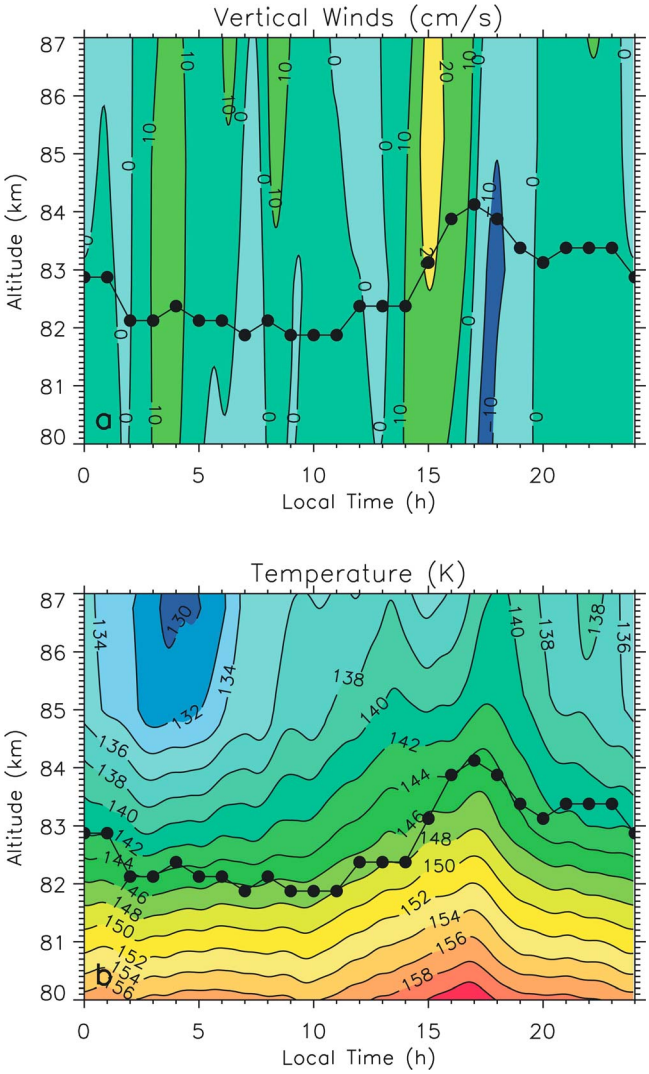

Figure 4. (a) Time-height cross section of vertical winds (contour labels in cm/s) in the upper mesosphere from the NOGAPS-ALPHA analysis averaged over June 2007 at 69°N. The winds are directed both upward and downward with the strongest upwelling near 0300 and 1500 LT, as indicated in Figure 2c. Calculated PMC altitudes are shown, indicating the strong correlation with vertical winds. (b) Same as in Figure 4a, but for temperature (contour labels in K).

and Thomas [2006], although modified to use the time-dependent inputs along its trajectory as described above. We use the same eddy diffusion as recommended by Rapp and Thomas and do not vary it with LT. Ice properties are saved from the last time step at each hour of LT from a fixed (target) latitude for comparison to observations over the diurnal cycle at that latitude.

[24] The NOGAPS-ALPHA temperature, water vapor, and vertical winds are provided in 1° longitude increments, equivalent to every 4 min in LT. Although the microphysics is recalculated every 100 s, the time increment over which CARMA is updated with new temperature and vertical wind profiles is therefore every 240 s. The water vapor is initialized once, using the relevant profile for the target local time and latitude, and allowed to redistribute so that the water vapor responds to vertical transport rather than horizontal transport. The vertical grid spacing for NOGAPS-ALPHA is about 2 km and this output is interpolated onto the finer (0.25 km) grid of CARMA.

[25] We assume that cosmic smoke is the nucleation source of all the ice particles and initialize the model once with the distribution reported for mid-June at 74°N by *Bardeen et al.* [2010]. These model smoke results show that it is depleted in the summer polar mesosphere due to relatively rapid equatorward transport [*Megner et al.*, 2008; *Bardeen et al.*, 2008], in agreement with SOFIE smoke observations [*Hervig et al.*, 2009c].

[26] We have chosen to investigate PMC IWC since it is a vertically integrated property, thereby avoiding the need to accurately simulate the peak of a narrow ice layer, and since it is relatively insensitive to variations in the ambient conditions other than temperature and water vapor [*Rapp and Thomas*, 2006, Table 1]. We first present a sensitivity study showing how IWC varies depending on the modeling approach. Specifically, we show how IWC varies with fixed ambient conditions, with variations over latitude and LT and with varying ice particle lifetimes. These simulations focus on results near 2300 LT since this corresponds to the SOFIE observations. The SOFIE IWC is an average for June 2007 (39 μg/m^2), but we increase this by 39% (54 μg/m^2) based on the reported latitudinal variation of ice mass from the average SOFIE latitude (66°N) in June to 69°N [*Stevens et al.*, 2007].

[27] Figure 6 shows a variety of CARMA simulations in which we have varied the assumptions used in the calculation of IWC. Each of the simulations in Figure 6 is integrated for 48 h, but only results for the last 24 h are shown. Because the IWC is a function of the ice particle growth rate and the particle lifetime, we introduce a warm bias to the ambient temperatures and remove the bias in different ways as described below. The water vapor profile for all simulations in Figure 6 is initialized once and allowed to redistribute vertically through freeze drying.

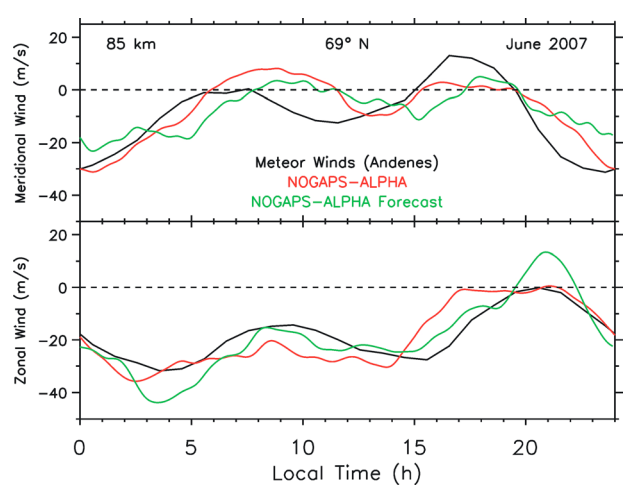

Figure 5. A comparison of (top) meridional and (bottom) zonal winds from the NOGAPS-ALPHA analysis and the NOGAPS-ALPHA forecast with ground based meteor wind observations during the same June 2007 time period at the geometric altitude of 85 km.

[28] Figure 6a shows an IWC simulation where the ambient temperature is given a 30 K warm bias and then abruptly set to the temperature profile at 69°N and 2300 LT, after which the ice particles are allowed to nucleate and grow over a period of 24 h. This simple approach also uses a constant vertical wind profile from 69°N and therefore neglects all effects of diurnal variations and horizontal transport from higher latitudes. For the simulation in Figure 6a, we calculate an IWC of 140 μg/m^2 at the end of the final 24 h. *Rapp and Thomas* [2006] use the same approach of a "cold start" with a fixed temperature and vertical wind profile to calculate the IWC. Although they did not use the same temperatures, vertical winds, water vapor, or meteoric smoke as our simulation, they nonetheless find an IWC of 135 μg/m^2 for their reference case after 24 h, very similar to our calculated value. These results are however a factor of ~2.5 larger than the SOFIE observation indicated in Figure 6a. *Bardeen et al.* [2010] used the three-dimensional Whole-Atmosphere Community Climate Model (WACCM) with microphysics from CARMA to derive an IWC of 12–51 μg/m^2 at 66°N and 2300 LT, in good agreement with the SOFIE observations for June 2007.

[29] Figure 6b shows the results of two simulations, each of which includes the effects of transport from higher latitudes. The variations of LT and latitude over one day of elapsed time are indicated on the upper axes of this panel. In one case, we have started the ice formation abruptly with the temperature and vertical wind profiles starting 24 h prior and run the simulation for 24 h while continuously updating these profiles along the trajectory. This yields an IWC that is about a factor of 4 larger than the SOFIE observation.

[30] This "cold start" approach, whereby CARMA is initialized from a highly supersaturated state and with clouds growing quickly, is likely unrealistic. It is more likely that clouds grow more slowly as the air starts out subsaturated, then cools, and becomes progressively more saturated. Unfortunately we cannot fully address this since our microphysical model is not coupled to the background atmosphere (as in the work of *Bardeen et al.* [2010]). Furthermore, there is little observational data as to the time history of the PMCs. Instead, our approach is to simply assume the air is subsaturated and apply a progressively decreasing temperature bias along the parcel trajectory. To fit the SOFIE observations, we set this cooling rate to

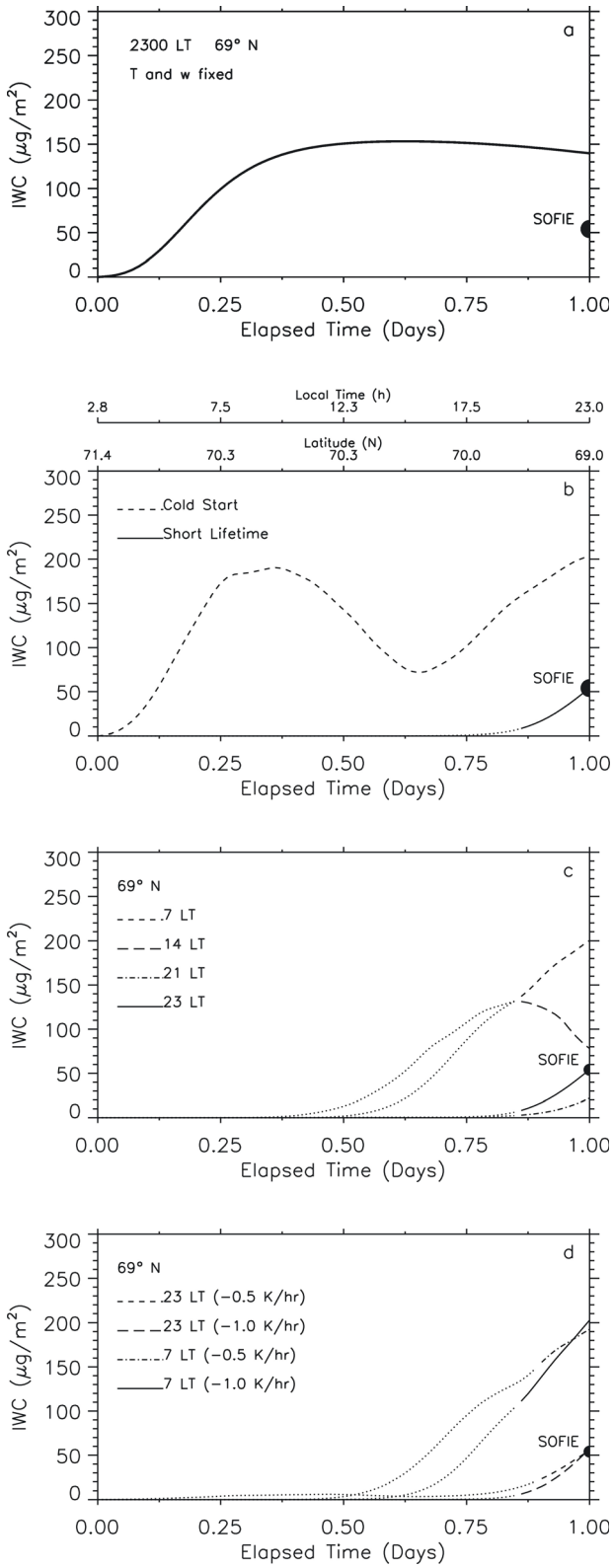

Figure 6. (a) The calculated time variation of IWC. NOGAPS-ALPHA temperature, water vapor, and vertical wind profiles are used for 69°N and 2300 LT. The temperature and vertical wind profiles are fixed. (b) Two simulations showing the variation of IWC with latitude and LT for an ice particle advected through ambient temperatures and vertical winds to 69°N. The dashed line shows a 24 h simulation where the temperature profiles from NOGAPS-ALPHA are used throughout ("Cold Start"). The solid line introduces a temperature bias that is gradually removed (see text), thereby reducing the ice particle growth and the IWC ("Short Lifetime"). The dotted portion of the Short Lifetime case indicates the time period during which the ambient conditions have not yet been reached. (c) Similar to the Short Lifetime case of Figure 6b except three other LTs are added for comparison. The indicated LTs correspond to the last time step of each simulation. (d) The IWC variation at 2300 and 0700 LT using two different cooling rates from an initial temperature bias: −0.5 K/h (22.8 K bias) and −1.0 K/h (44.4 K bias). The temperature biases are selected so that the SOFIE data at 2300 LT is fit.

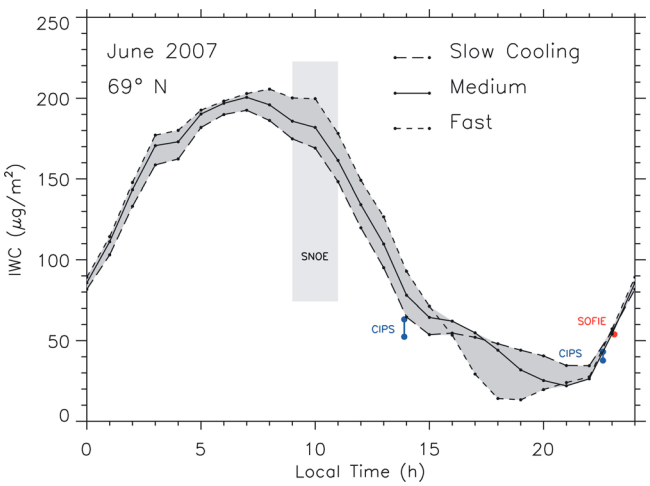

Figure 7. The calculated IWC over the diurnal cycle at 69°N for June 2007. Three different solutions are presented representing three assumed parcel cooling rates: slow (0.50 K/h), medium (0.68 K/h), and fast (1.00 K/h), where the shading represents the range within these solutions (see text). AIM/CIPS (blue) and AIM/SOFIE (red) data from the same time period are overplotted. The CIPS observations are averaged over a 3° latitude band around 69°N and have been scaled up to be consistent with simultaneous SOFIE observations in separate common volume observations. Also shown are observations from SNOE, which were collected between 0900 and 1100 LT and have been scaled upwards for representative solar minimum conditions.

-0.68 K/h from an initial temperature bias of +30 K at all altitudes in Figure 6b. The ice particles are therefore subjected to ambient conditions for only 3–4 h out of a total of 48 h of microphysics. We note that this effective ice particle lifetime of 3–4 h is an order of magnitude smaller than the ice particle lifetime inferred by *Berger and von Zahn* [2007], who instead derived their lifetime from the observed size distribution at the peak of the ice layer at 69°N. However, the particle lifetime used herein is consistent with the more recent study of *Zasetsky et al.* [2009], who argued that particles form in 2–20 h. As indicated in Figure 6b, longer lifetimes increase the IWC beyond the SOFIE observations for our June 2007 case study at 2300 LT.

[31] Figure 6c shows the results for simulations at four different LTs: 0700 LT, 1400 LT, 2100 LT, and 2300 LT. 0700 LT and 2100 LT are chosen because they yield the maximum and minimum IWC over the diurnal cycle, respectively, 1400 LT is chosen because it corresponds to some of the CIPS observations (discussed in section 3) and 2300 LT corresponds to the SOFIE observations reproduced from Figure 6b. Figure 6c illustrates that the simulations that end at 0700 and 1400 LT produce clouds earlier than the others, but that the ambient conditions are reached at the same point in each simulation. The IWC is largest at 0700 LT because this is just after the low temperature phase of the diurnal cycle and IWC is smallest at 2100 LT because this is just after the time of highest temperatures (see Figure 4).

[32] The cooling rate (−0.68 K/h) and the temperature bias (+30 K) used in Figure 6c are selected to yield a solution consistent with SOFIE at 2300 LT. However, other combinations of these two parameters can also fit the SOFIE data. We herein also consider cooling rates of −0.5 and −1.0 K/h to assess the impact on the resultant IWC, consistent with representative rates for heterogeneous nucleation as discussed in the recent work of *Murray and Jensen* [2010] that bracket our baseline case. These cooling rate changes vary the exposure time to conditions which favor growth. The temperature biases for these two cases are chosen to fit the SOFIE data at 2300 LT at the end of each 48 h integration. Figure 6d shows the results for a −0.5 K/h cooling rate (+22.8 K bias) and −1.0 K/h cooling rate (+44.4 K bias) at 2300 LT and also at the maximum IWC at 0700 LT. The IWC at 0700 LT are very similar, and we consider the effects of these different cooling rates over the entire diurnal cycle in section 3.

3. Diurnal IWC Simulations

3.1. Results for 69°N

[33] Figure 7 shows the calculated IWC at each hour of LT over the diurnal cycle. For each of the 24 simulations, the temperatures and the vertical winds were specified along a trajectory defined by the horizontal winds and ending at the local time of interest. The water vapor is initialized once for each LT at 69°N and allowed to redistribute vertically through freeze drying, as for the simulations in Figure 6. In addition to our baseline case shown in Figure 6c, we include results with more cooling and less cooling as discussed in section 2. The shaded area in Figure 7 shows the range of solutions at each LT from the three different simulations. As with the PMC altitudes shown in Figure 4, a comparison of the IWC variation over the diurnal cycle with ground-based observations from a single location is misleading because the ice particles observed at one location can be subject to processes that we cannot reproduce with our approach. We instead compare the simulated IWC to zonally averaged satellite observations measuring at discrete LT.

[34] On Figure 7 there are also two zonally averaged observations of IWC from CIPS (version 3.20 retrievals) [see *Rusch et al.*, 2009; *Benze et al.*, 2009], which measures near 1350 and 2240 LT in the Northern Hemisphere on the descending and ascending nodes of the AIM orbit, respectively. SOFIE is a solar occultation instrument and sensitively measures the IWC directly whereas CIPS is a nadir imager and less sensitive, so we have applied an upward adjustment to the CIPS data using separate common volume (CV) observations [*Russell et al.*, 2009]. This upward adjustment is discussed further below.

[35] Near 69°N, SOFIE and CIPS execute observations that are specifically coordinated to observe the same volume of ice. We define the average IWC from these CV observations as the vertical integral of the ice mass density through a cloud, multiplied by the cloud frequency during June 2007. In the case of CIPS, the cloud frequency is determined by the number of CIPS pixels in which a cloud was detected divided by the total number of CIPS pixels along the SOFIE line of sight. For SOFIE, the cloud frequency is the number of occultations in which a cloud was detected divided by the total number of occultations. Using this approach, SOFIE yields an IWC consistently higher than CIPS because many clouds along the SOFIE line of sight are below the CIPS detection threshold.

[36] To account for the reduced sensitivity of CIPS, we scale the CIPS CV IWC up to the SOFIE CV IWC. However, we do not know independently how much IWC is below the CIPS threshold away from the CV. We therefore calculate a scale factor for the undetectable ice in two ways: one scale factor (4.9) assumes that the observations with no PMCs are indeed clear air and one (1.9) assumes that these observations are at the CIPS threshold. We find that the average CIPS IWC threshold is 18 μg/m^2, which corresponds on average to a CIPS directional albedo threshold of 5×10^{-6} sr^{-1}. To be consistent with this approach in the CV, at 69°N we assign values of zero where there is clear air and use the scale factor of 4.9 for one solution and the smaller scale factor of 1.9 for the other solution. The results are shown in Figure 7, and on average the CIPS IWC near 1400 LT is 58 μg/m^2 whereas the IWC near 2300 LT is 31% smaller at 40 μg/m^2. The agreement of the scaled CIPS data with the simulations in Figure 7 is good, although these data do not significantly help to validate the large dynamic range of the IWC simulated by CARMA using NOGAPS-ALPHA analyses because CIPS does not make measurements at those LTs when our model predicts a large IWC.

[37] To help validate the larger morning IWC, we use observations from SNOE near 1000 LT. SNOE was launched into a Sun-synchronous orbit in February 1998 and observed PMCs for nearly six years over both poles [*Bailey et al.*, 2005]. *Stevens et al.* [2007] inferred the PMC ice mass from SNOE observations in the Arctic from the cloud brightnesses and occurrence frequencies. The reported SNOE ice mass for midsolar cycle conditions at 70°N is equivalent to an IWC of 53–106 μg/m^2, depending on the ice particle size distribution. Since the study here focuses on solar minimum conditions and since PMCs are known to be brighter and more frequent at solar minimum, we apply an upward correction to this IWC, which is described below.

[38] Several studies have calculated the solar cycle variation of ice content (sometimes called H_2O(ice)), ice mass or IWC, which all scale the same way. *Siskind et al.* [2005] reported a ratio of the ice content from solar minimum to maximum of a factor of 3 near 70°N, which they regarded as a likely upper limit. *Stevens et al.* [2007] used SBUV data to show that the variation of ice mass is at least a factor of 2 over the solar cycle. Using these studies, we therefore take the solar cycle variation of IWC to range from a factor of 2–3 from solar maximum to solar minimum. We note that this is somewhat greater than the IWC variation over the solar cycle inferred in the modeling study of *Bardeen et al.* [2010], who determined that at solar minimum the IWC is 1.44 times greater than at solar maximum. To conservatively represent the range of possible solutions, we therefore apply a factor of 1.4 for our lower IWC limit from midsolar cycle to solar minimum and a factor of 2.1 for our upper IWC limit to solar minimum. We find that the scaled SNOE observations range from 74 to 223 μg/m^2. This is the range overplotted in Figure 7 and is in agreement with the IWC calculation. The calculated difference between the IWC near 1000 LT where SNOE observes and near 2300 LT where SOFIE observes is a factor of 3.4. This underscores the importance of including tidally induced IWC variations when comparing data sets with each other and with model results.

[39] To our knowledge, Figure 7 shows results of the first PMC IWC calculation over the diurnal cycle and has important implications for reconciling two or more sets of PMC observations at discrete LT. In general, the IWC has a maximum between 0700 and 0800 LT and a minimum between 1900 and 2200 LT with a variation exceeding a factor of 5 Additional ground-based or satellite observations of IWC over the diurnal cycle would greatly help us to constrain the variability indicated by the simulations. Analysis of the Southern Hemisphere as well as other seasons and latitudes would also help to determine how representative these results are. We now consider observations from the same June 2007 time period at 57°N.

3.2. Results for Subpolar Latitudes

[40] One additional data set that can be used to validate the NOGAPS-ALPHA/CARMA simulations is from the SHIMMER instrument [*Stevens et al.*, 2009]. SHIMMER retrievals do not include IWC versus LT but SHIMMER nonetheless observed two pronounced occurrence frequency peaks near 0600 LT and 1800 LT during the NH summer 2007. We show the calculated IWC at 57°N in Figure 8a, where we have initialized the model with the smoke distribution from *Bardeen et al.* [2010] at 58°N, included water vapor freeze drying as in Figure 7 and used the same ice particle lifetime as in Figure 6c.

[41] Figure 8a shows a strong IWC peak near 0500 LT in good agreement with the SHIMMER frequency peak near 0600 LT. Variations in the assumed ice particle lifetime change the absolute IWC of the 0500 LT peak, but the pronounced variation of the IWC calculated over the diurnal cycle does not change. Simulations that include LT variations at 57°N latitude and without meridional transport yield no clouds at all. We conclude that this early morning peak is therefore due to either southward meridional transport from higher latitudes where the air is colder (Figure 2b) [e.g., *Gerding et al.*, 2007] or transient colder periods near the temperature minimum not reflected in the monthly average.

[42] The second SHIMMER peak near 1800 LT does not appear in the simulation of average June 2007 conditions due to the higher temperatures and subsaturated air during this time of day. However, average conditions may not be representative for the relatively low cloud frequencies observed by SHIMMER, which are less than 5% averaged over all LT for the northern 2007 summer [*Stevens et al.*, 2009]. We herein consider the possibility that the second peak in Figure 8a may be the result of temperatures occasionally falling below the frost point, even though the monthly average would not reflect such cold temperatures. We represent this variability by the standard deviation of the NOGAPS-ALPHA temperatures at 83 km altitude for the month of June. Figure 8b shows the degree of supersaturation (S) at 83 km altitude as well as S after subtracting the standard deviation from NOGAPS-ALPHA temperatures during each indicated LT. The SHIMMER PMC observations were made between 50°N and 58°N, so we use 54°N as a representative latitude for our analysis of supersaturation. As one can see, when the temperature falls below the average consistent with the standard deviation of the variability the air can often be supersaturated with values locally peaking near three at 1800 LT. We note that there is equa-

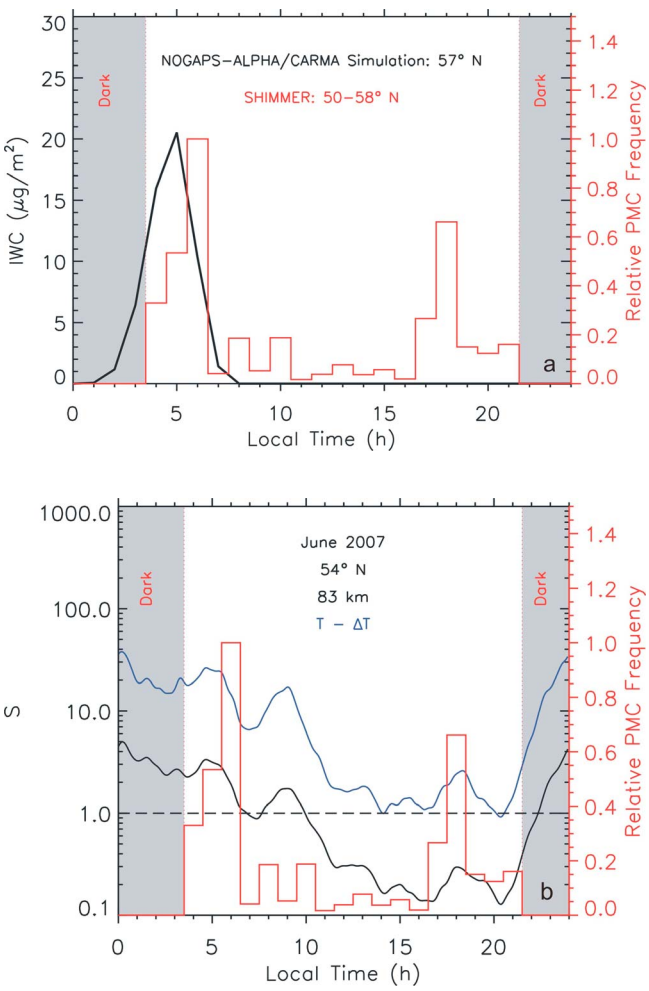

Figure 8. (a) The calculated IWC at 57°N for June 2007 (black). Also shown for comparison is the observed relative PMC frequency during NH 2007 from SHIMMER [*Stevens et al.*, 2009]. The shaded region indicates where there is not enough sunlight for SHIMMER to reliably infer the frequency. (b) Calculated degree of supersaturation (S) over the diurnal cycle at 54°N and 83 km geometric altitude (black). Ice particles can exist where $S > 1$. The blue curve indicates the degree of supersaturation after subtraction of the standard deviation of the temperature. The SHIMMER relative frequencies from Figure 8a are again overplotted in red and referenced to the right hand axis.

torward flow until about 1500 LT (Figure 2b) with a meridional wind reversal near this time so that a peak in cloud frequency might also be expected near this time from equatorward transport. The NOGAPS-ALPHA analysis indicates therefore that conditions can often be favorable for the appearance of clouds at 1800 LT even though the monthly average result in Figure 8a does not show this.

4. Discussion

[43] Our study on tidally induced variations of PMC IWC for June 2007 approaches the problem in three new ways. First, we have chosen to simulate the IWC rather than cloud brightness or frequency for four reasons: (1) IWC is a direct measure of how much ice is present, (2) it is a vertically integrated quantity and therefore does not require simulation of a narrow ice layer peak, (3) it is primarily sensitive to only temperature and water vapor [*Rapp and Thomas*, 2006], and (4) it is measured directly by SOFIE on the AIM satellite. Second, we have used meteorological analysis fields from a global numerical weather prediction system that has recently been extended to ~90 km altitude. This allows us to specify temperature, water vapor, and winds over the diurnal cycle for a specific time period during which we have PMC data. Third, we drive the one-dimensional version of CARMA with time varying NOGAPS-ALPHA input to simulate PMC altitude variations and IWC over the diurnal cycle. Specification of assimilated ambient conditions with latitude and LT more realistically represents the ice particle's history than either a free running climate model or a microphysical model with a constant temperature profile as is sometimes done. We assume that only cosmic smoke particles serve as nucleation sites for the clouds and that clouds formed in any other way contribute negligibly to the total IWC at any given LT.

[44] One limitation of this study is that it uses assimilated data from only the month of June 2007, which may not represent typical June conditions. To address this limitation, we have continued the NOGAPS-ALPHA assimilation configuration described in the work of *Eckermann et al.* [2009] through the 2009 PMC season and assembled the temperatures for three consecutive Junes on a zonally averaged LT grid. Figure 9 shows the variation of temperature over the diurnal cycle at 83 km geometric altitude for June 2007, 2008, and 2009 at three different latitudes: 81°N (Figure 9a), 69°N (Figure 9b), and 57°N (Figure 9c). The consistency of the assimilated temperatures from one year to the next is remarkable and on average the temperature is about 10 K lower at 81°N compared to 57°N.

[45] With respect to the temperatures over the diurnal cycle, we draw several important conclusions from Figure 9: (1) the migrating diurnal tide dominates LT temperature variability throughout the Arctic mesosphere in June from 2007 to 2009; (2) the average amplitude of the tidal temperature oscillation is repeatable at any given latitude for this time period and the time of the maximum varies between 1400 and 2000 LT at all latitudes; (3) the amplitude becomes progressively larger at lower latitudes with an amplitude of ~2 K at 81°N to ~5 K at 57°N; and (4) the temperature variability at a given LT also becomes progressively larger at lower latitudes with a standard deviation of 3–6 K at 81°N and 5–8 K at 57°N. We conclude from Figure 9 that the diurnal variation of temperatures for our June 2007 simulation is representative for solar minimum conditions at all latitudes. Since we find that the diurnal variation of temperatures primarily controls the IWC variation, we also conclude that the calculated IWC over the diurnal cycle shown in Figure 7 is also representative of solar minimum conditions.

[46] Ultimately, our analysis suggests that our work may have the greatest utility in interpreting data from different satellites which are in Sun-synchronous orbits fixed in LT. As we noted in the introduction, the SBUV series of instruments has viewed PMCs for over 30 years, which is the longest PMC time series available. These nadir-viewing observations are typically reported as albedo (unitless) but

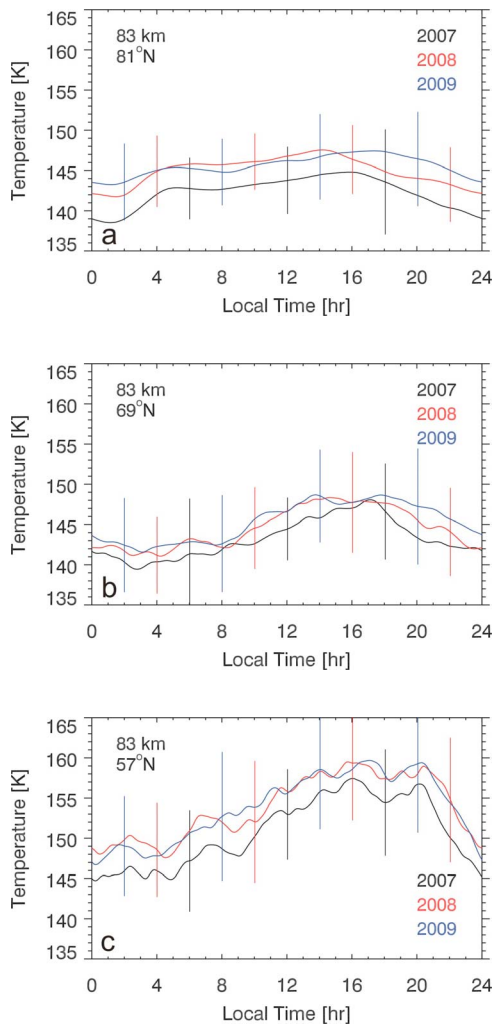

Figure 9. (a) The variation of temperature over the diurnal cycle for June 2007–2009 at 83 km geometric altitude and 81°N. The vertical bars represent the standard deviation of the assimilated temperatures within the monthly averages. (b) Same as in Figure 9a, except for 69°N. (c) Same as in Figure 9a, except for 57°N.

are actually directional albedo (sr^{-1}) at 252 nm, with multidecadal trends of less than 1%/yr. Figure 10 shows the variation of directional albedo at 252 nm for each hour of LT using the same CARMA size distributions as the IWC calculations in Figure 6c. We calculate the albedo at a variety of relevant SBUV solar scattering angles (SSAs) from 90° to 150°. Away from the terminator ($\theta > 90°$), the average calculated albedo in Figure 10 is between 0.2 and 3×10^{-5} sr^{-1}, consistent with the albedo typically reported for SBUV of about 1×10^{-5} sr^{-1} [e.g., *DeLand et al.*, 2006].

[47] Figure 10 illustrates that the calculated albedo variation over the diurnal cycle is similar to the IWC variation, with a peak between 0600 and 0800 LT and a minimum between 1900 and 2100 LT. The largest variations over the diurnal cycle reported heretofore are in cloud occurrence frequency, which are implicitly included in our averaged model results. Large variations in cloud frequency over the diurnal cycle with a prominent peak in the morning were reported in both ground-based and SBUV data sets [*Fiedler et al.*, 2005; *Shettle et al.*, 2009].

[48] It is well known that the mid-UV PMC albedo is a function of the SSA [*van de Hulst*, 1981], and we note the SBUV SSA is the supplement of the solar zenith angle. The curves show that the albedo is significantly larger at the terminator ($\theta = 90°$) than for lower solar zenith angles at a given LT. This means that a comparison of SBUV albedo and/or frequency observations not only requires consideration of the LT but also the SSA, particularly when the observations are near local sunrise and sunset. Importantly, the calculated albedo (or IWC) maximizes in the morning which corresponds to the average LT of the SBUV observations between 1979 and 1990 after which the observations are more uniformly spread over the diurnal cycle [*DeLand et al.*, 2007]. If the June 2007 results in Figure 10 are representative of all northern PMC seasons within the multidecadal SBUV data set, this implies that inferred long-term PMCs trends of albedo or IWC would increase following adjustment due to diurnal variations.

5. Summary

[49] In summary, we have produced the first quantitative simulation of IWC over the diurnal cycle at 57°N and 69°N using assimilated satellite data from June 2007. The simulation at 69°N is constrained by concurrent observations from SOFIE, which measures IWC directly near 23 LT. The IWC has a diurnal variation that is controlled by the migrating diurnal temperature tide and the peak IWC is between 0500 and 0800 LT at both 57°N and 69°N.

[50] The relative variation in IWC over the diurnal cycle is larger at the equatorward fringe of the PMC region, significantly complicating the interpretation of multidecadal trends reported at these latitudes [*DeLand et al.*, 2007]. Even at 69°N, however, the IWC or mid-UV albedo varies

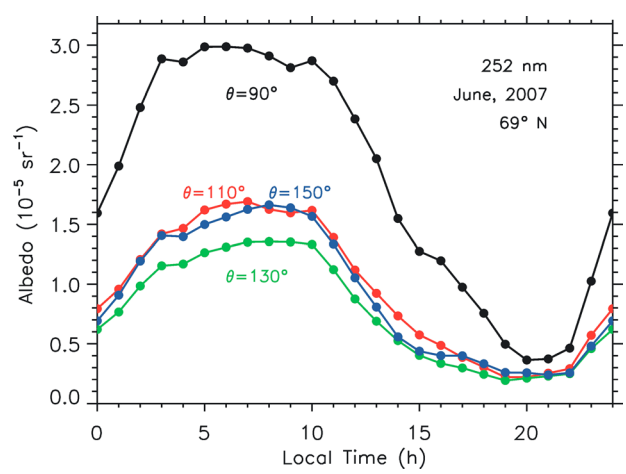

Figure 10. Calculated PMC directional albedos for observations at 252 nm at a variety of SSAs (θ) relevant to the SBUV data set. The calculations assume spherical particles and use the same particle size distributions as the IWC calculations in Figure 6c. For the nadir-viewing geometry of SBUV, the solar zenith angle is equal to 180°–θ so that $\theta = 90°$ is representative of observations at the Earth's terminator.

by at least a factor of 5, with a peak between 0700 and 0800 LT and a minimum between 1900 and 2200 LT. Careful consideration of not only the LT but also the latitude for any given set of observations must therefore precede any IWC trend analysis.

[51] Our description of IWC over the diurnal cycle currently lacks experimental validation. Ground-based observations of the PMC frequency at 69°N show a factor of 4 variation with a peak near 1 LT [*Fiedler et al.*, 2005]. Limited satellite observations of PMC frequency are consistent with a factor of 3 variation during the morning with a maximum near 2 LT [*Shettle et al.*, 2009]. Modeling work by *Jensen et al.* [1989] showed that the PMC brightness varied by up to a factor of 7 over the diurnal cycle depending on the amplitude of the temperature variations, with a maximum near 23 LT that follows a temperature minimum near 20 LT. Although none of these studies report the IWC variation over the diurnal cycle, taken together they illustrate that variations of related quantities can be between a factor of 3 and 7. Our derived variation of at least a factor of 5 in IWC at 69°N is therefore not unreasonable in the context of these previous studies. Our inferred maximum between 0700 and 0800 LT is, however, between 5 and 9 h later than these results would indicate. Direct temperature observations near 83 km altitude over the diurnal cycle in addition to any IWC observations would provide a useful comparison to the results presented here.

[52] **Acknowledgments.** This work was supported by the NASA/AIM mission and the Office of Naval Research. We thank Gary Thomas for useful comments on the manuscript and Charles Bardeen for providing the meteoric smoke concentrations used in this work. We are also grateful to Fabrizio Sassi for assistance with the NOGAPS-ALPHA analysis.

References

Bailey, S. M., A. W. Merkel, G. E. Thomas, and J. N. Carstens (2005), Observations of polar mesosphere clouds by the Student Nitric Oxide Explorer, *J. Geophys. Res.*, *110*, D13203, doi:10.1029/2004JD005422.

Bailey, S. M., A. W. Merkel, G. E. Thomas, and D. W. Rusch (2007), Hemispheric differences in Polar Mesospheric Cloud morphology observed by the Student Nitric Oxide Explorer, *J. Atmos. Sol.-Terr. Phys.*, *69*, 1407–1418.

Bardeen, C. G., O. B. Toon, E. J. Jensen, D. R. Marsh, and V. L. Harvey (2008), Numerical simulations of the three-dimensional distribution of meteoric dust in the mesosphere and upper stratosphere, *J. Geophys. Res.*, *113*, D17202, doi:10.1029/2007JD009515.

Bardeen, C. G., O. B. Toon, E. J. Jensen, M. E. Hervig, C. E. Randall, S. Benze, D. R. Marsh, and A. Merkel (2010), Numerical simulations of the three-dimensional distribution of polar mesospheric clouds and comparisons with Cloud Imaging and Particle Size (CIPS) experiment and the Solar Occultation For Ice Experiment (SOFIE) observations, *J. Geophys. Res.*, *115*, D10204, doi:10.1029/2009JD012451.

Benze, S., C. E. Randall, M. T. DeLand, G. E. Thomas, D. W. Rusch, S. M. Bailey, J. M. Russell III, W. McClintock, A. W. Merkel, and C. Jeppesen (2009), Comparison of polar mesospheric cloud measurements from the Cloud Imaging and Particle Size experiment and the Solar Backscatter Ultraviolet Instrument in 2007, *J. Atmos. Sol.-Terr. Phys.*, *71*, 365–372.

Berger, U., and F.-J. Lübken (2006), Weather in mesospheric ice layers, *Geophys. Res. Lett.*, *33*, L04806, doi:10.1029/2005GL024841.

Berger, U., and U. von Zahn (2002), Ice particles in the summer mesopause region: Three-dimensional modeling of their environment and two-dimensional modeling of their transport, *J. Geophys. Res.*, *107*(A11), 1366, doi:10.1029/2001JA000316.

Berger, U., and U. von Zahn (2007), Three-dimensional modeling of the trajectories of visible noctilucent cloud particles: An indication of particle nucleation well below the mesopause, *J. Geophys. Res.*, *112*, D16204, doi:10.1029/2006JD008106.

Chu, X., C. S. Gardner, and R. G. Roble (2003), Lidar studies of interannual, seasonal, and diurnal variations of polar mesospheric clouds at the South Pole, *J. Geophys. Res.*, *108*(D8), 8447, doi:10.1029/2002JD002524.

Chu, X., P. J. Espy, G. J. Nott, J. C. Diettrich, and C. S. Gardner (2006), Polar mesospheric clouds observed by an iron Boltzmann lidar at Rothera (67.5°S, 68.0°W), Antarctica from 2002 to 2005: Properties and implications, *J. Geophys. Res.*, *111*, D20213, doi:10.1029/2006JD007086.

DeLand, M. T., E. P. Shettle, G. E. Thomas, and J. J. Olivero (2003), Solar backscattered ultraviolet (SBUV) observations of polar mesosphereic clouds (PMCs) over two solar cycles, *J. Geophys. Res.*, *108*(D8), 8445, doi:10.1029/2002JD002398.

DeLand, M. T., E. P. Shettle, G. E. Thomas, and J. J. Olivero (2006), A quarter-century of satellite polar mesospheric cloud observations, *J. Atmos. Sol.-Terr. Phys.*, *68*, 9–29.

DeLand, M. T., E. P. Shettle, G. E. Thomas, and J. J. Olivero (2007), Latitude-dependent long-term variations in polar mesospheric clouds from SBUV version 3 PMC data, *J. Geophys. Res.*, *112*, D10315, doi:10.1029/2006JD007857.

Eckermann, S. D., K. W. Hoppel, L. Coy, J. P. McCormack, D. E. Siskind, K. Nielsen, A. Kochenash, M. H. Stevens, C. R. Englert, and M. Hervig (2009), High-altitude data assimilation system experiments for the northern summer mesosphere season of 2007, *J. Atmos. Sol.-Terr. Phys.*, *71*, 531–551.

Englert, C. R., M. H. Stevens, D. E. Siskind, J. M. Harlander, F. L. Roesler, H. M. Pickett, C. von Savigny, and A. J. Kochenash (2008), First results from the Spatial Heterodyne Imager for Mesospheric Radicals (SHIMMER): Diurnal variation of mesospheric hydroxyl, *Geophys. Res. Lett.*, *35*, L19813, doi:10.1029/2008GL035420.

Fiedler, J., G. Baumgarten, and G. von Cossart (2005), Mean diurnal variations of noctilucent clouds during 7 years of lidar observations at ALOMAR, *Ann. Geophys.*, *23*, 1175–1181.

Gerding, M., J. Höffner, M. Rauthe, W. Singer, M. Zecha, and F.-J. Lübken (2007), Simultaneous observation of noctilucent clouds, mesospheric summer echoes and temperature at a midlatitude station (54°N), *J. Geophys. Res.*, *112*, D12111, doi:10.1029/2006JD008135.

Gordley, L. L., et al. (2009), The Solar Occultation For Ice Experiment (SOFIE), *J. Atmos. Sol.-Terr. Phys.*, *71*, 300–315.

Herbort, F., G. Baumgarten, U. Berger, J. Fiedler, P. Hoffmann, and F. J. Lübken (2007), Tidal structures within the LIMA model, *Adv. Space Res.*, *40*, 802–808.

Hervig, M. E., L. L. Gordley, J. M. Russell III, and S. M. Bailey (2009a), SOFIE PMC observations during the northern summer of 2007, *J. Atmos. Sol.-Terr. Phys.*, *71*, 331–339.

Hervig, M. E., M. H. Stevens, L. L. Gordley, L. E. Deaver, J. M. Russell III, and S. M. Bailey (2009b), Relationships between PMCs, temperature and water vapor from SOFIE observations, *J. Geophys. Res.*, *114*, D20203, doi:10.1029/2009JD012302.

Hervig, M. E., L. L. Gordley, L. E. Deaver, D. E. Siskind, M. H. Stevens, J. M. Russell III, S. M. Bailey, L. Megner, and C. G. Bardeen (2009c), First satellite observations of meteoric smoke in the upper atmosphere, *Geophys. Res. Lett.*, *36*, L18805, doi:10.1029/2009GL039737.

Hoffmann, P., M. Rapp, J. Fiedler, and R. Latteck (2008), Influence of tides and gravity waves on layering processes in the polar summer mesopause region, *Ann. Geophys.*, *26*, 4013–4022.

Hogan, T. F., and T. E. Rosmond (1991), The description of the Navy Operational Global Atmospheric Predication System's spectral forecast model, *Mon. Weather Rev.*, *119*, 1786–1815.

Hoppel, K. W., N. L. Baker, L. Coy, S. D. Eckermann, J. P. McCormack, G. E. Nedoluha, and D. E. Siskind (2008), Assimilation of stratospheric and mesospheric temperatures from MLS and SABER into a global NWP model, *Atmos. Chem. Phys.*, *8*, 6103–6116.

Jensen, E., G. E. Thomas, and O. B. Toon (1989), On the diurnal variation of noctilucent clouds, *J. Geophys. Res.*, *94*, 14693–14702, doi:10.1029/JD094iD12p14693.

Kirkwood, S., P. Dalin, and A. Rechon (2008), Noctilucent clouds observed from the UK and Denmark – Trends and variations over 43 years, *Ann. Geophys.*, *26*, 1243–1254.

Klostermeyer, J. (1998), A simple model of the ice particle size distribution in noctilucent clouds, *J. Geophys. Res.*, *103*, 28,743–28,752, doi:10.1029/98JD02070.

Kwon, K. H., C. S. Gardner, D. C. Senft, F. L. Roesler, and J. Harlander (1987), Daytime lidar measurements of tidal winds in the mesospheric sodium layer at Urbana, Illinois, *J. Geophys. Res.*, *92*, 8781–8786, doi:10.1029/JA092iA08p08781.

Lambert, A., et al. (2007), Validation of the Aura Microwave Limb Sounder middle atmosphere water vapor and nitrous oxide measurements, *J. Geophys. Res.*, *112*, D24S36, doi:10.1029/2007JD008724.

Lübken, F.-J. (1999), Thermal structure of the Arctic summer mesosphere, *J. Geophys. Res.*, *104*, 9135–9149, doi:10.1029/1999JD900076.

Lübken, F.-J., and U. Berger (2007), Interhemispheric comparison of mesospheric ice layers from the LIMA model, *J. Atmos. Sol.-Terr. Phys.*, *69*, 2292–2308.

Lübken, F.-J., G. Baumgarten, J. Fiedler, M. Gerding, J. Hoffner, and U. Berger (2008), Seasonal and latitudinal variation of noctilucent cloud altitudes, *Geophys. Res. Lett.*, *35*, L06801, doi:10.1029/2007GL032281.

Lübken, F.-J., U. Berger, and G. Baumgarten (2009), Stratospheric and solar cycle effects on long term variability of mesospheric ice clouds, *J. Geophys. Res.*, *114*, D00I06, doi:10.1029/2009JD012377.

Marti, J., and K. Mauersberger (1993), A survey and new measurements of ice vapor pressure at temperatures between 170 and 250 K, *Geophys. Res. Lett.*, *20*, 363–366, doi:10.1029/93GL00105.

McClandress, C. (2002), The seasonal variation of the propagating diurnal tide in the mesosphere and lower thermosphere: Part I. The role of gravity waves and planetary waves, *J. Atmos. Sci.*, *59*(5), 893–906.

Megner, L., J. Gumbel, M. Rapp, and D. E. Siskind (2008), Reduced meteoric smoke particle density at the summer pole – Implications for mesospheric ice particle nucleation, *Adv. Space Res.*, *41*, 41–49.

Murray, B. J., and E. J. Jensen (2010), Homogeneous nucleation of amorphous solid water particles in the upper mesosphere, *J. Atmos. Sol.-Terr. Phys.*, *72*, 51–61.

Rapp, M., and G. E. Thomas (2006), Modeling the microphysics of mesospheric ice particles: Assessment of current capabilities and basic sensitivities, *J. Atmos. Sol.-Terr. Phys.*, *68*, 715–744.

Remsberg, E. E., et al. (2008), Assessment of the quality of the version 1.07 temperature-versus-pressure profiles of the middle atmosphere from TIMED/SABER, *J. Geophys. Res.*, *113*, D17101, doi:10.1029/2008JD010013.

Rusch, D. W., G. E. Thomas, W. McClintock, A. W. Merkel, S. M. Bailey, J. M. Russell III, C. E. Randall, C. Jeppesen, and M. Callan (2009), The cloud imaging and particle size experiment on the aeronomy of ice in the mesosphere mission: Cloud morphology for the northern 2007 season, *J. Atmos. Sol.-Terr. Phys.*, *71*, 356–364.

Russell, J. M., III, et al. (2009), The Aeronomy of Ice in the Mesosphere (AIM) mission: Overview and early science results, *J. Atmos. Sol.-Terr. Phys.*, *71*, 289–299.

Schwartz, M. J., et al. (2008), Validation of the Aura Microwave Limb Sounder temperature and geopotential height measurements, *J. Geophys. Res.*, *113*, D15S11, doi:10.1029/2007JD008783.

Shettle, E. P., M. T. DeLand, G. E. Thomas, and J. J. Olivero (2009), Long-term variations in the frequency of polar mesospheric clouds in the Northern Hemisphere from SBUV, *Geophys. Res. Lett.*, *36*, L02803, doi:10.1029/2008GL036048.

Singer, W., J. Bremer, W. K. Hocking, J. Weiss, R. Latteck, and M. Zecha (2003), Temperature and wind tides around the summer mesopause at middle and Arctic latitudes, *Adv. Space Res.*, *31*(9), 2055–2060.

Siskind, D. E., M. H. Stevens, and C. R. Englert (2005), A model study of global variability in mesospheric cloudiness, *J. Atmos. Sol.-Terr. Phys.*, *67*, 501–513.

Stevens, M. H., C. R. Englert, M. T. DeLand, and M. Hervig (2005), The polar mesospheric cloud mass in the Arctic summer, *J. Geophys. Res.*, *110*, A02306, doi:10.1029/2004JA010566.

Stevens, M. H., C. R. Englert, M. T. DeLand, and S. M. Bailey (2007), Polar mesospheric cloud mass and the ice budget: 2. Application to satellite data sets, *J. Geophys. Res.*, *112*, D08205, doi:10.1029/2006JD007532.

Stevens, M. H., C. R. Englert, M. Hervig, S. V. Petelina, W. Singer, and K. Nielsen (2009), The diurnal variation of polar mesospheric cloud frequency near 55°N observed by SHIMMER, *J. Atmos. Sol.-Terr. Phys.*, *71*, 401–407.

Thomas, G. E. (1996), Is the polar mesosphere the miner's canary of global change?, *Adv. Space Res.*, *18*, 149–158.

Thomas, G. E., and C. P. McKay (1985), On the mean particle size and water content of polar mesospheric clouds, *Planet. Space Sci.*, *33*, 1209–1224.

Thomas, G. E., J. J. Olivero, E. J. Jensen, W. Schroeder, and O. B. Toon (1989), Relation between increasing methane and the presence of ice clouds at the mesopause, *Nature*, *338*, 490–492.

Thomas, G. E., J. J. Olivero, M. T. DeLand, and E. P. Shettle (2003), Comment on "Are noctilucent clouds truly a 'miner's canary' for global change", *EOS*, *84*(36), 351.

van de Hulst, H. C. (1981), *Light Scattering by Small Particles*, Dover Publications, Inc., New York.

von Zahn, U., and U. Berger (2003), Persistent ice cloud in the midsummer upper mesosphere at high latitudes: Three-dimensional modeling and cloud interactions with ambient water vapor, *J. Geophys. Res.*, *108*(D8), 8451, doi:10.1029/2002JD002409.

von Zahn, U., and J. Bremer (1999), Simultaneous and common-volume observations of noctilucent clouds and polar mesosphere summer echoes, *Geophys. Res. Lett.*, *26*, 1521–1524, doi:10.1029/1999GL900206.

von Zahn, U., G. von Cossart, J. Fiedler, and D. Rees (1998), Tidal variations of noctilucent clouds measured at 69°N latitude by ground-based lidar, *Geophys. Res. Lett.*, *25*, 1289–1292, doi:10.1029/98GL00546.

Zasetsky, A. Y., S. V. Petelina, R. Remerov, C. D. Boone, P. F. Bernath, and E. J. Llewelyn (2009), Ice particle growth in the polar summer mesosphere: Formation time and equilibrium size, *Geophys. Res. Lett.*, *36*, L15803, doi:10.1029/2009GL038727.

S. M. Bailey, Bradley Department of Electrical and Computer Engineering, Virginia Polytechnical and State University, Blacksburg, VA 24061, USA.

L. Coy, S. D. Eckermann, C. R. Englert, J. P. McCormack, D. E. Siskind, and M. H. Stevens, Space Science Division, Naval Research Laboratory, 4555 Overlook Ave. SW, Washington, DC 20375, USA.

M. E. Hervig, GATS, Inc., Driggs, ID 83422, USA.

P. Hoffmann and M. Rapp, Leibniz Institute of Atmospheric Physics, Schlossstr. 6, D-18225 Kühlungsborn, Germany.

K. W. Hoppel, Remote Sensing Division, Naval Research Laboratory, 4555 Overlook Ave. SW, Washington, DC 20375, USA.

A. J. Kochenash and K. Nielsen, Computational Physics, Inc., Springfield, VA, USA.

J. Lumpe, Computational Physics, Inc., 1650 38th St., 105W, Boulder, CO 80301, USA.

C. E. Randall, Laboratory for Atmospheric and Space Physics and Department of Atmospheric and Oceanic Sciences, University of Colorado, Boulder, CO 80309, USA.